

行政院原子能委員會
委託研究計畫研究報告

常壓非熱電漿滅菌裝置之模擬研究(2/3 年)
Simulation of Atmospheric-pressure Plasma for
Sterilization (2/3Year)

計畫編號：992001INER028

受委託機關(構)：國立交通大學

計畫主持人：吳宗信

核研所聯絡人員：陳永枝

聯絡電話：(03)5712121-31693

E-mail address：chongsin@faculty.nctu.edu.tw

報告日期：99/12/21

Table of Contents

| | |
|--|-----------|
| TABLE OF CONTENTS | |
| 中文摘要 | I |
| ABSTRACT | II |
| 1. BACKGROUN AND MOTIVATION | 1 |
| 2. NUMERICAL METHOD AND PROCEDURES | 5 |
| 2.1 NAVIER-STOCK EQUATIONS SOLVER | 5 |
| 2.2 PLASMA FLUID MODELING | 11 |
| 3. RESULTS AND CONCLUSIONS | 16 |
| 3.1 ATMOSPHERIC PRESSURE ONE-DIMENSION HELIUM DBD | 16 |
| 3.2 .ATMOSPHERIC PRESSURE ONE-DIMENSION NITROGEN DBD | |
| | 26 |
| 3.3 ATMOSPHERIC PRESSURE TWO-DIMENSION HE AND NITROGEN | |
| DBD | 31 |
| 4. CONCLUSIONS | 34 |
| 5. REFERENCES | 35 |
| 6. PUBLICATIONS | 37 |

中文摘要

非熱電漿技術應用於生醫領域上為近年來之熱門研究課題，目前之趨勢已由早期低壓電漿應用，逐漸轉向常壓大氣電漿技術之開發。而大氣電漿滅菌機制、反應器設計(間接或直接電漿)及最佳操作條件等均尚處於研究階段中，其中大多以實驗探討之，缺點是耗時長以及成本高。一般來說，電漿模擬亦相當耗時。另鑑於近年來高速電腦設備之急遽增加與普及，平行處理計算技術提升，提供了常壓電漿模擬技術上重大進展的機會。唯平行計算應用於非熱電漿的模擬，仍屬少見，甚為可惜。因此，本計劃在此針對此常壓非熱電漿滅菌裝置進行模擬，以求達到最佳化設計，提供實驗設計參考，以利核能研究所在非熱電漿技術研發及在生醫領域上之應用與推廣。第二年預定工作將包括： 1. 建立有限差分方法(FDM)之二維及二維軸對稱模擬平行計算模組，計算電漿粒子能量分布。2. 加入二維及二維軸對稱 Navier-Stoke equation 模組計算中性氣體及自由基的流場分布。3. 探討不同電漿氣體流速、電源功率與電極電壓等參數間與自由基產生量、種類、及時空分布情形之相互關聯性。4. 提供電漿滅菌反應器一最佳化參數，供實驗設計參考。

ABSTRACT

In recent years, non-thermal plasma technology in the biomedical fields in recent years become popular. The current trend is from early low-pressure plasma gradually shift to the development of atmospheric plasma technology. The experimental studies of atmospheric plasma sterilization system still rely on trial-and-error, which is time-consuming and costly. In general, plasma simulation is also very time consuming. Fortunately, rapid advance of the high-performance computing and parallel technology provide opportunities for plasma simulation techniques. However, parallel computing applied studies of non-thermal plasma are still rare. This study for the non-thermal plasma at atmospheric pressure sterilization device simulation conducted in order to achieve the best design, providing experimental design reference. In order to facilitate the Institute of Nuclear Energy Research in the development and biomedical fields in the application on and promotion. The goals of 2nd Year project are: 1) to develop a 2D/2D axisymmetric finite difference method fluid modeling code to calculate plasma properties distribution. 2) to couple with 2D/2D axisymmetric Navier-Stokes equations solver for solving the neutral and radical species distribution. 3) to discuss the species densities and spatial-temporal distribution in differential operating conditions such as flow rate, applied voltage and power. 4) to estimate the optimized parameters for plasma sterilization.

1. Background and Motivation

Conventional sterilization technologies, such as autoclaves, ovens, chemicals such as ethylene oxide (EtO), and radiation (gamma rays) [1, 2] heavily rely on the irreversible metabolic inactivation or breakdown of vital structural components of microorganisms. Although some of these methods which apply direct heating may be effective in inactivating microorganisms, they are often highly inefficient in terms of time and cost (high energy consumption). Sterilization/inactivation using non-thermal plasmas represents one of the most promising technologies. Most applications of plasma technology for sterilization/inactivation require the direct contact of the discharge with the bacterial cells [3] because abundant chemically active ions, electrons and radicals exist in the discharge. The use of low-pressure plasma may be helpful, whereby the electrode distance can be quite large. A larger space between the electrodes in low-pressure plasmas means easier handling of the treated bacteria, as compared to those using atmospheric-pressure plasmas [4, 5], in which the electrode distance is very small (order of mm). However, handling the test pieces requires the break of the vacuum, which is costly and time-consuming.

Deng et. al has show a 10-min exposure to the atmospheric-helium plasma plume led to a 4-log reduction of the *Bacillus subtilis* spores, whereas the use of the less than 0.2-log reduction [4]. Lee et. al has show D-values were 14 min for *B. subtilis* spore. The sterilizing effect of the Atmospheric-pressure cold helium/oxygen plasma is not due to UV light, which is known to be the major sterilization factor of APCP, but instead results from the action of reactive oxygen radicals [5]. Lerouge's group investigated *B. subtilis* spore

sterilization by O₂/CF₄ plasma under low-pressure condition, which exhibited much higher efficacy than all other gases or gas mixtures tested (O₂, O₂/Ar, O₂/H₂ and CO₂), with more than a 5 log decrease in 7.5 min, as compared with a 2 log decrease with pure oxygen at an operation pressure of 80 mTorr [6]. Note B. subtilis spore represents one of the toughest organisms, which can tolerate extreme environmental conditions for more than 10 years, and has been often used as a target bacterium to test whether the sterilization method is effective or not. However, the creation of low-pressure plasmas requires the use of vacuum equipment, which is very expensive and rather impractical in bio-medical applications.

Recently, sterilization/inactivation using non-thermal atmospheric-pressure plasmas (APP) has attracted tremendous attention [7, 8]. The major advantages of applying atmospheric-pressure plasmas may include, among others [9]: 1) generating abundant bactericidal active agents (chemically active radicals, high kinetic energy ions, electrons, and UV photons); 2) producing a fairly low-temperature gas stream which is in direct contact with the bacteria or container; 3) a shorter operating time in the order of seconds or minutes; 4) easy removal of inactivated bacteria and viruses on the treated surface through jet gas streams; and 5) producing essentially no hazardous substances.

Recently, simulation has become an important method in understanding the plasma physics and chemistry of gas discharges since the direct quantitative measurements inside the discharge volume are either very difficult or very costly. Not only can an efficient and

accurate modeling provide detailed plasma physics and chemistry within complex gas discharges, but also may it be used as an optimization tool for designing a new plasma source.

Among these developed numerical tools for gas discharges simulation, fluid modeling is one of the fastest yet accurate methods, if the pressure is not too low (e.g., >50 mtorr), which can greatly help the understanding of the plasma physics and chemistry. However, to cope with practical gas discharge problems, multidimensional simulations (2 to 3 spatial dimensions) using complex plasma chemistry (large number of species and reaction channels) are often required to understand the insight of the plasmas. However, it often takes up to weeks or even months to complete a meaningful fluid modeling simulation, which is of course unacceptable from the practical viewpoint of being a useful tool. In addition, developed fluid modeling codes were often lack of extensive experimental validations, which may further prevent its use in industry from being a practical tool in helping the design of gas discharge related devices.

Fortunately, recent rapid advance in computer hardware and parallel computing (multicore CPU and GPU) over the past two decades may help to reduce the runtime of a typical plasma simulation. In addition, complex yet flexible software design has become possible by taking advantage of different programming approaches such as OpenMP and MPI through high-level computer languages like C/C++ and Fortran. Concept like object-oriented design pattern further aids in the task of designing of complex software.

Excellent performance capability has been demonstrated through the development of efficient numerical schemes, such as the finite difference, finite element, and finite volume methods, and algorithms, such as Krylov subspace method for iteratively solving discretized equations. Combining progress in plasma physics, scientific computing, storage capacities and calculation speeds, could lead to the development of a simulation tool to help researchers understand the physics and chemistry of plasmas, design plasma equipment and to reduce costs associated with the current trial-and-error approach.

In this report we intend to develop a parallelized plasma simulation tool for sterilization. The goals are: 1) to develop a 2D/2D axisymmetric finite difference method fluid modeling code to calculate plasma properties distribution. 2) to couple with 2D/2D axisymmetric Navier-Stoke equations solver for solving the neutral and radical species distribution. 3) to discuss the species densities and spatial-temporal distribution in differential operating conditions such as flow rate, applied voltage and power. 4) to estimate the optimized parameters for plasma sterilization.

2. Numerical Method

2.1. Navier-Stock Equations Solver

2.1.1 Governing Equations

The general form of mass conservation, Navier-Stokes equation, energy conservation equations can be recast in the Cartesian tensor form as follows:

$$\frac{\partial(\rho\phi)}{\partial t} + \frac{\partial}{\partial x_j}(\rho V_j \phi) = \frac{\partial}{\partial x_j} \left(\mu_\phi \frac{\partial \phi}{\partial x_j} \right) + S_\phi \quad (1)$$

where t is the time, x is the coordinate, V is the velocity, and the subscript j can take the value 1, 2, 3, denoting the three space coordinates. μ_ϕ is an effective diffusion coefficient, S_ϕ is the source term, ρ is the fluid density and $\phi = (1, u, v, h_t)$ stands for the variables for the mass, momentum, and energy equations, respectively.

2.1.2 Numerical Scheme

2.1.2.1 Spatial Discretization

The transport equations using the cell-centered finite-volume scheme can be written generally in integral form as

$$\frac{\partial}{\partial t} \int_{\Omega} \rho \phi d\Omega + \int_{\Gamma} \vec{F} \cdot \vec{n} d\Gamma = \int_{\Omega} S_\phi d\Omega \quad (2)$$

where Ω is the domain of interest, Γ is the surrounding surface, and \vec{n} is the unit normal in outward direction. The time derivative is calculated using the first-order forward difference scheme, and the source term is treated using last time step value. The flux function \vec{F} consists of the inviscid and the viscous parts:

$$\vec{F} = \rho \vec{V} \phi - \mu_\phi \nabla \phi \quad (3)$$

The finite volume formulation of flux integral can be evaluated by the summation of the flux vectors over each face,

$$\int_{\Gamma} \vec{F} \cdot \vec{n} d\Gamma = \sum_{j=k(i)} F_{i,j} \Delta\Gamma_j \quad (4)$$

where $k(i)$ is a list of faces of cell i , $F_{i,j}$ represents convection and diffusion fluxes through the interface between cell i and j , $\Delta\Gamma_j$ is the cell-face area. The viscous flux for the face e between control volumes P and E as shown in Figure 1 can be approximated as:

$$\nabla \phi_e = \frac{\phi_E - \phi_P}{|\vec{x}_E - \vec{x}_P|} = \frac{\phi_E - \phi_P}{\Delta x_{P,E}} \quad (5)$$

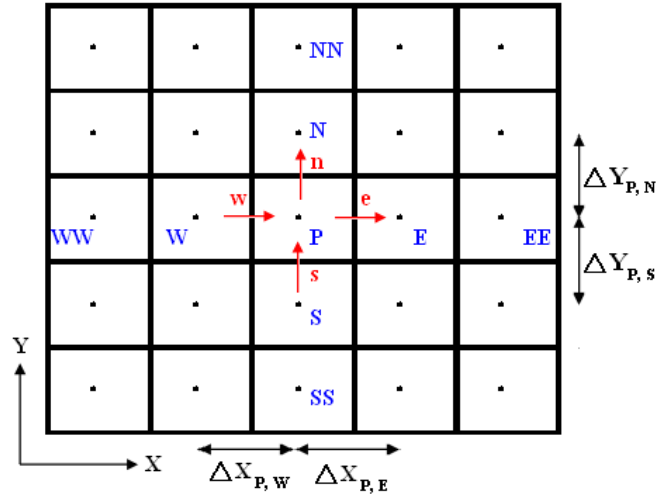


Figure 1: Two-dimensional control volume.

2.1.2.2 Upwind Scheme

The inviscid flux is evaluated through the values at the upwind cell and a linear reconstruction procedure to achieve second order accuracy as

$$\phi_e = \phi_u + \Psi_e \nabla \phi_u \cdot (\vec{x}_e - \vec{x}_u) \quad (6)$$

where the subscript e and u represents interface and the upwind cell, respectively, and Ψ_e

is a flux limiter used to prevent from local extrema introduced by the data reconstruction.

Defining $\phi_{\max} = \max(\phi_u, \phi_j)$ and $\phi_{\min} = \min(\phi_u, \phi_j)$, where ϕ_j is the neighbor cell of upwind cell, the Ψ_e associated with the gradient at cell u due to edge e is

$$\Psi_e = \begin{cases} \min\left(1, \frac{\phi_{\max} - \phi_u}{\phi_e^0 - \phi_u}\right), & \text{if } \phi_e^0 - \phi_u > 0 \\ \min\left(1, \frac{\phi_{\min} - \phi_u}{\phi_e^0 - \phi_u}\right), & \text{if } \phi_e^0 - \phi_u < 0 \\ 1, & \text{if } \phi_e^0 - \phi_u = 0 \end{cases} \quad (7)$$

where ϕ_e^0 is computed without the limiting condition (i.e. $\Psi_e = 1$).

2.1.2.3 Pressure Smoothing

The cell face velocity u_e is usually obtained by linear interpolation as

$$u_e = \frac{1}{2}(u_E + u_P) \quad (8)$$

To avoid the pressure oscillations due to simulation on a collocation grid, the face velocity can be modified as [10]

$$u_e = \frac{1}{2}(u_E + u_P) + \left(\frac{\partial P}{\partial x} \frac{\delta \Omega}{A}\right)_{e1} - \left(\frac{\partial P}{\partial x} \frac{\delta \Omega}{A}\right)_{e2} \quad (9)$$

where A is the coefficient in the discretized momentum equation.

The first pressure gradient term is calculated as the mean value of cell P and E ,

$$\begin{aligned} \left(\frac{\partial P}{\partial x} \frac{\delta \Omega}{A}\right)_{e1} &= \frac{1}{2} \left(\left(\frac{\partial P}{\partial x}\right)_E + \left(\frac{\partial P}{\partial x}\right)_P \right) \left(\frac{\delta \Omega}{A}\right)_e \\ &= \frac{1}{2} \left(\frac{P_{EE} - P_P}{\delta x_{P,EE}} + \frac{P_E - P_W}{\delta x_{W,E}} \right) \left(\frac{\delta \Omega}{A}\right)_e \end{aligned} \quad (10)$$

The second one is calculated on the edge,

$$-\left(\frac{\partial P}{\partial x} \frac{\delta \Omega}{A}\right)_{e2} = -\left(\frac{P_E - P_P}{\delta x_{P,E}}\right) \left(\frac{\delta \Omega}{A}\right)_e \quad (11)$$

Set $\delta x_{P,EE} = \delta x_{W,E} = 2\delta x_{P,E}$ and

$$u_e = \frac{1}{2}(u_E + u_P) + \frac{1}{4\delta x_{P,E}} \left(\frac{\delta \Omega}{A}\right)_e [P_{EE} - 3P_E + 3P_P - P_W] \quad (12)$$

which is used to calculate the convection flux through the control volume faces. The first term is treated as a weighted average, and the second one is kept as it is to deal with non-equidistant grids.

2.1.2.4 Velocity-Slip and Temperature-Jump Boundary Conditions

The velocity-slip boundary condition is given as:

$$v_s - v_w = \zeta \left. \frac{\partial v}{\partial n} \right|_s \quad (13)$$

where v_s is the velocity of gas at the solid wall surface, v_w is the velocity of wall, $\zeta = 1.1466 \cdot Kn_{local} = 1.1466 \cdot Kn / \rho_{local}$, Kn_{local} is the local Knudsen number, ρ_{local} in the local density, and $\left. \frac{\partial v}{\partial n} \right|_s$ is the derivative of velocity normal to the wall surface [11]. The

temperature-jump is treated in a similar way:

$$T_s - T_w = \tau \left. \frac{\partial T}{\partial n} \right|_s \quad (14)$$

where T_s is the temperature of gas at the solid wall surface, T_w is the temperature of wall,

$\tau = 2.1904 \cdot Kn_{local} = 2.1904 \cdot Kn / \rho_{local}$, and $\left. \frac{\partial T}{\partial n} \right|_s$ is the derivative of temperature normal to the wall surface [11].

2.1.2.5 Solution Procedure

A general implicit discretized time-marching scheme for the transport equations is employed to solve the discretized equations. It can be written as:

$$\left(\frac{\rho^n}{\Delta t} + A_p \right) \phi_p^{n+1} = \sum A_{NB} \phi_{NB}^{n+1} + \frac{(\rho \phi_p)^n}{\Delta t} + S_\phi^n \quad (15)$$

where the superscripts n and $n+1$ mean old value (at time t) and new value (at time $t+dt$) of the variables, respectively. The high order differencing terms and cross diffusion terms are treated using known quantities and retained in the source term and updated explicitly.

In an extended SIMPLE [12, 13] family pressure-correction algorithm, the pressure correction equation for all-speed flows is formulated using the perturbed equation of state, momentum and continuity equations. The simplified formulations can be written as

$$\rho' = \frac{p'}{RT} \quad (16a)$$

$$u'_m = -D_u \nabla p' \quad (16b)$$

$$u^{k+1} = u^k + u' \quad (16c)$$

$$p^{k+1} = p^k + p' \quad (16d)$$

$$\frac{\partial \rho}{\partial t} + \nabla(u_m \rho') + \nabla(\rho u'_m) = -\nabla(\rho u_m)^k \quad (17)$$

where R is the ideal gas constant, u_m is the m^{th} Cartesian component of the velocity, and D_u is the pressure-velocity coupling coefficient. Substituting Eq.(16) into Eq.(17), and considering $\Delta \rho = \rho^{k+1} - \rho^n = (\rho^{k+1} - \rho^k) + (\rho^k - \rho^n) = \rho' + (\rho^k - \rho^n)$, the following all-speed pressure correction equation is obtained,

$$\frac{1}{RT} \frac{p'}{\Delta t} + \nabla \left(\frac{u_m}{RT} p' \right) - \nabla(\rho D_u \nabla p') = - \left(\frac{\rho^k - \rho^n}{\Delta t} \right) - \nabla(\rho u_m)^k \quad (18)$$

where the superscript k represents the last iterative value.

For the cell-centered scheme, the flux integration is conducted along each face and its contribution is sent to the two cells on either side of the interface. Once the integration loop is performed along the face index, the discretization of the governing equations is completed. First, the momentum equation is solved implicitly at the predictor step. Once the solution of pressure-correction equation is obtained, the velocity, pressure and density fields are updated. The predictor-corrector step is repeated 2 and 3 times so that the mass conservation is enforced. Then, the solution procedure marches to the next time level for transient calculations or global iteration for steady-state calculations. A basic description of the simulation processes is available in Figure 2. In addition, parallel computing is implemented and tested on distributed-memory machines using spatial domain decomposition.

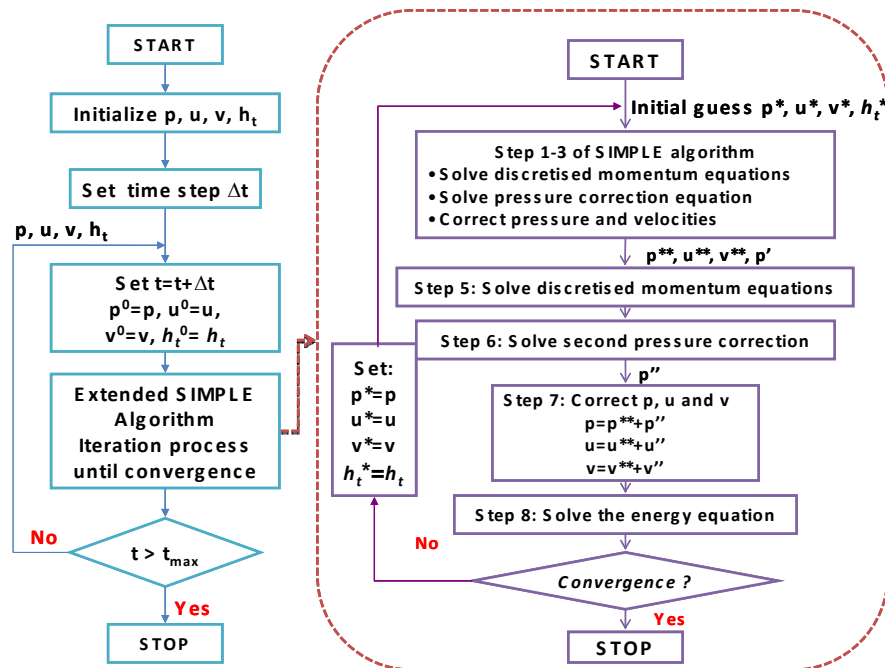


Figure 2: Flowchart of the extended SIMPLE algorithm.

2.2. Plasma Fluid Modeling

In the framework of fluid modeling, electron and ion number densities are calculated as functions of time and space resulting from the coupled solution of species continuity equation, species momentum equation, species energy equation, and field equations. Since the fluid modeling equations are similar for most of the gas discharges, we only summarize a typical set of equations in the following as the model equations for the purpose of demonstration. Note that we neglect flow convection effects in the present study.

The general continuity equation for ion species can be written as,

$$\frac{\partial n_p}{\partial t} + \vec{\nabla} \cdot \vec{\Gamma}_p = \sum_{i=1}^{r_p} S_{p_i} \quad p=1, \dots, K \quad (19)$$

where n_p is the number density of ion species p , K is the number of ion species, r_p is the number of reaction channels that involve the creation and destroy of ion species p , and $\vec{\Gamma}_p$ is the particle flux that is expressed as, based on the drift-diffusion approximation,

$$\vec{\Gamma}_p = \text{sign}(q_p) \mu_p n_p \vec{E} - D_p \vec{\nabla} n_p \quad (20)$$

$$\vec{E} = -\nabla \phi \quad (21)$$

where q_p , \vec{E} , μ_p , D_p and α_{iz} are the ion charge, the electric field, the electron mobility, the electron diffusivity, and the ionization rate, respectively. Note that the form of source term S_{p_i} can be modified according to the modeled reactions describing how the ion species p is generated or destroyed in reaction channel i . Boundary conditions at walls are applied considering thermal diffusion, drift and diffusion fluxes.

The continuity equation for electron species e can be written as,

$$\frac{\partial n_e}{\partial t} + \vec{\nabla} \cdot \vec{\Gamma}_e = \sum_{i=1}^{r_e} S_{e_i} \quad (22)$$

where n_e is the number density of ions, r_e is the number of reaction channels that involve the creation and destroy of electron, and $\vec{\Gamma}_e$ is the corresponding particle flux that is expressed as, based on drift-diffusion approximation,

$$\vec{\Gamma}_e = -\mu_e n_e \vec{E} - D_e \vec{\nabla} n_e \quad (23)$$

where μ_e and D_e are the electron mobility and electron diffusivity, respectively. These two transport coefficients can be readily obtained as a function of electron temperature from the solution of a publicly available computer code for the Boltzmann equation, named BOLSIG+ [15]. Similar to S_{P_i} , the form of S_{e_i} can also be modified according to the modeled reactions which generate or destroy the ion in reaction channel i. Boundary conditions at walls are applied considering thermal diffusion, drift and diffusion fluxes of electrons. Secondary electron emission or photo-electron emission from the solid walls can be readily added if necessary.

Continuity equation for neutral species can be written as,

$$\frac{\partial n_{uc}}{\partial t} + \vec{\nabla} \cdot \vec{\Gamma}_{uc} = \sum_{i=1}^{r_{uc}} S_{uc_i} \quad uc=1, \dots, L \quad (24)$$

where n_{uc} is the number density of uncharged species uc, L is the number of neutral species, r_{uc} is the number of reaction channels that involve the creation and destroy of uncharged species uc and $\vec{\Gamma}_{uc}$ is the corresponding particle flux, neglecting convection

effects, which can be expressed as

$$\vec{\Gamma}_{uc} = -D_{uc} \vec{\nabla} n_{uc} \quad (25)$$

where D_{uc} is the diffusivity of neutral species. Similarly, the form of S_{uc_i} can also be modified according to the modeled reactions which generate or destroy the species in reaction channel i . Neumann boundary conditions at walls are applied since no surface reactions are considered in the present study.

Electron energy density equation can be expressed as,

$$\frac{\partial n_{\varepsilon}}{\partial t} + \nabla \cdot \vec{\Gamma}_{n_{\varepsilon}} = -e \vec{\Gamma}_e \cdot \vec{E} - \sum_{i=1}^{s_e} \varepsilon_i S_i + 3 \frac{m_e}{M} n_e k_B \nu_m (T_e - T_g) \quad (26)$$

where $n_{\varepsilon} \left(= \frac{3}{2} n_e k_B T_e \right)$ is the electron energy density, T_e is the electron temperature, ε_i is the energy loss for the i th inelastic electron collision, k_B is the Boltzmann constant, ν_m is the momentum exchange collision frequency between electron (mass m_e) and background neutral (mass M), T_g is the background gas temperature, and $\vec{\Gamma}_{n_{\varepsilon}}$ is the corresponding electron energy density flux as,

$$\vec{\Gamma}_{n_{\varepsilon}} = \frac{5}{2} k_B T_e \vec{\Gamma}_e - \frac{5}{2} \frac{n_e k_B T_e}{m_e \nu_m} \nabla (k_B T_e) \quad (27)$$

The second term on the right-hand side of eq. (26) represents the sum of the energy losses of electrons due to inelastic collision with other species. The last term on the right-hand side of eq. (26) can be ignored for low-pressure gas discharges, while it is important for medium-to-atmospheric pressure discharges. Similarly, boundary conditions at walls are applied considering thermal diffusion, drift and diffusion fluxes. Secondary

electron emission and other boundary effects can be readily added if needed.

Poisson's equation for electrostatic potential can be expressed as

$$\nabla \cdot (\varepsilon \nabla \varphi) = -\left(\sum_{i=1}^K q_i n_i - en_e\right) \quad (28)$$

where φ is the potential and ε is a function of position, whose value is either the vacuum or dielectric permittivity depending upon the problem. All the transport properties of neutral and ions are obtained from literature data [16][17].

Discretization, Numerical Schemes and Algorithms

In the present study, the above equations were recast into one-dimensional form and discretized using the finite-difference method, which is similar to our previous work [18] using a library of PETSc [19], except the addition of the electron energy density equation, which considers the effect of non-local electron transport. Resulting system of nonlinear algebraic equations was then solved using a fully implicit backward Euler's method in the temporal domain with the Scharfetter-Gummel scheme for the mass fluxes on the spatial domain. At each time step, the resulting algebraic nonlinear system is solved by a parallel fully coupled Newton-Krylov-Swartz (NKS) algorithm to solve the large sparse system of nonlinear discretized equations, where an additive Schwarz preconditioned GMRES is used for the solution of Jacobian system. We have used an inexact or exact solve such as incomplete LU (ILU) or LU factorizations in each subdomain for the preconditioning. We evaluated the Jacobian matrix entries using a hybrid analytical-numerical method, in which the entries involving the derivative with respect to number density (e.g., the source terms

of species continuity equations) are easily expressed analytically without resorting to numerical approximation. For other entries, it can be evaluated using a standard finite-difference method. This strategy is especially useful for the plasma simulations having a large number of species and reaction channels. Details of this implementation are presented elsewhere.

The transport coefficients and the rate constants related to electron were calculated by solving the Boltzmann equation using BOLSIG+ [15]. Note these coefficients were predicted and stored in a lookup table as a function of electron temperature. The transport coefficients (mobility and diffusivity) of ions (H^+ and He^{2+}) were adopted from those experiments by Mason et al. (1976) [17] as a function of reduced field (E/N) and were calculated by assuming species transport in helium background gas at a temperature 400 K. As for the diffusion coefficients of neutral species (atomic and molecular helium), they were the same as Yuan and Raja (2003) [16].

3. Results and Discussions

3.1. Atmospheric Pressure One-Dimension Helium DBD

The non-equilibrium atmospheric-pressure parallel-plate helium dielectric barrier discharge (DBD) driven by the realistic 20 kHz distorted-sinusoidal voltage waveform has been investigated by means of simulations and experiments. A self-consistent one-dimensional fluid modeling code considering the non-local electron energy balance was applied to simulate the helium DBD.

3.1.1 Comparison of Discharged Current between Simulation and Experiment

The input voltage waveform for simulations was obtained by Fourier series expansion of the measured voltage waveform across the electrodes using 50 terms of sine and cosine functions with 20 kHz as the fundamental frequency. The simulated temporal discharge currents along with the measurements are presented in Figure 3. Results show that the predicted temporal currents using the complex plasma chemistry are in excellent agreement with the measurements; while those using the simple plasma chemistry fail to reproduce the measurements during some periods in a cycle. This implies that inclusion of the more excited helium, metastable helium and electron-ion related detailed reaction channels is responsible for the successful fluid modeling of the helium AC DBD, which is different from the simulation of the helium RF discharge under atmospheric-pressure condition. In brief summary, the present fluid modeling code using the complex plasma chemistry can predict quantitatively the temporal evolution of discharged current of helium DBD driven by a 20 kHz distorted-sinusoidal power source very well, which is rarely

reported in the literature.

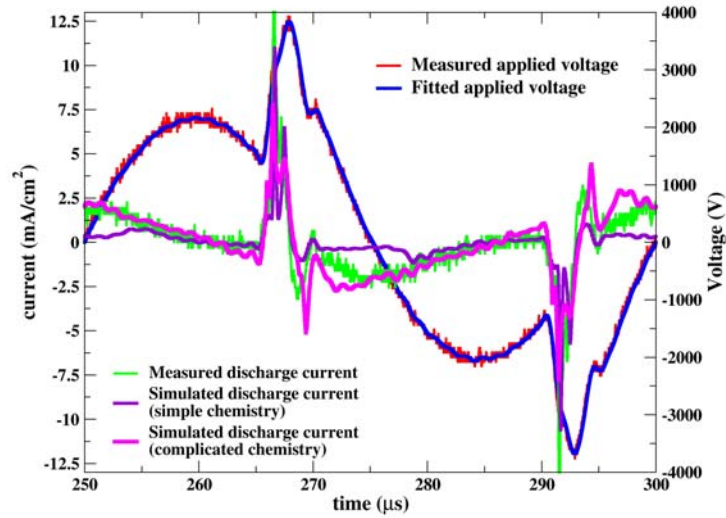


Figure 3. Comparison of simulated and measured discharge currents in a distorted-sinusoidal AC cycle (20 kHz).

3.1.2 Spatial Profiles of Cycle-averaged Plasma Properties

Figure 4 shows the cycle-average spatial power absorption by the plasma through various mechanisms. It shows that the molecular ions (He_2^+) absorb much more power through ohmic heating than the electrons do near both the dielectric surfaces, which is caused by the much higher concentration of the molecular ions than that of the electrons (~ 1 order), as can be seen clearly in Figure 3. Figure 3 illustrates the cycle-average spatial distribution of various plasma properties. It shows that the cycle-average number density of He_2^+ is much higher than that of the electrons (~ 1 order) and He^+ (2-3 orders), which leads to the observation that power absorption by the electrons and He^+ is small and

essentially negligible, respectively. This also confirms that it is a typical Townsend discharge in the average sense: much more ions exist than electrons.

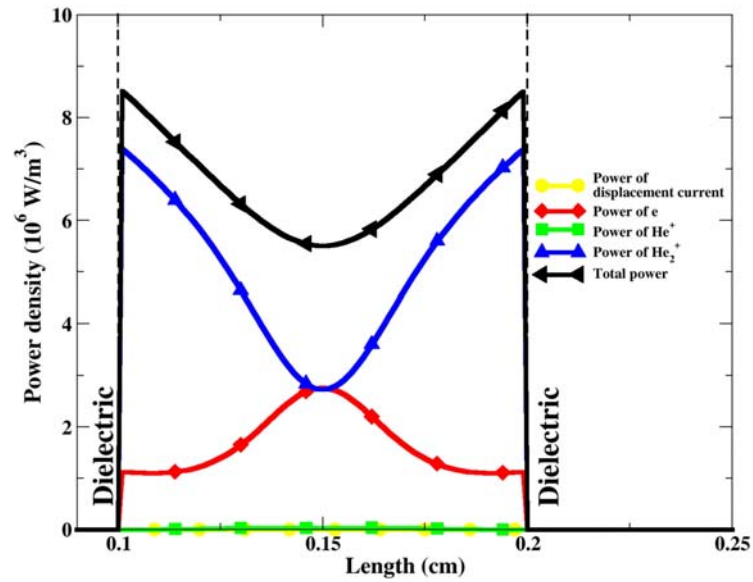


Figure 4. Time-averaged spatial power absorption by various mechanisms for the atmospheric-pressure helium DBD driven by a distorted-sinusoidal power source (20 kHz)

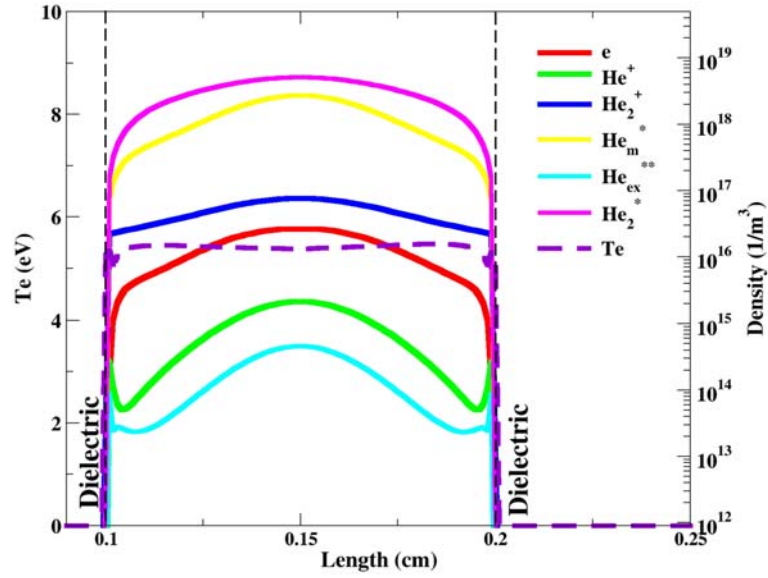


Figure 5. Spatial profiles of cycle-averaged discharge properties for the atmospheric-pressure helium DBD driven by a distorted-sinusoidal power source (20 kHz)

The average electron temperature is nearly uniform across the gap and is as high as 5.4 eV. The two most populated neutral species are metastable He_m^* and excimer He_2^* (or $\text{He}_2^* > \text{He}_m^* \gg \text{He}_{ex}^{**}$) mainly due to a series of ion-electron recombination, in addition to the direct electron-impact excitation, as shown in Table 1.

Table 1. Summary of simple and complicated helium plasma chemistry.

| N. | Reaction type | Reaction channels | Complicated* | Simple** | Threshold |
|----|---------------------|---|--------------|---|-----------|
| | | | | | (eV) |
| 00 | Momentum transfer | $e + \text{He} \rightarrow e + \text{He}$ | BOLSIG+ | BOLSIG+ | 0 |
| 01 | e-impact excitation | $e + \text{He} \rightarrow e + \text{He}_m^*$ | BOLSIG+ | $2.3 \times 10^{-16} T_e^{0.31} \exp\left(\frac{-2.29 \times 10^5}{T_e}\right)$ | 19.82 * |
| 02 | e-impact excitation | $e + \text{He} \rightarrow e + \text{He}_{ex}^{**}$ | BOLSIG+ | | 22.57 * |
| 08 | e-impact ionization | $e + \text{He} \rightarrow 2e + \text{He}^+$ | BOLSIG+ | $2.5 \times 10^{-18} T_e^{0.68} \exp\left(\frac{-2.85 \times 10^5}{T_e}\right)$ | 24.58 |

| | | | | | | |
|----|--|--|---------|--|-----------------------|-------|
| 09 | e-impact ionization | $e + \text{He}_m^* \rightarrow 2e + \text{He}^+$ | BOLSIG+ | $4.6 \times 10^{-16} T_e^{0.6} \exp\left(\frac{-5.546 \times 10^4}{T_e}\right)$ | 4.78 | |
| 10 | e-impact de-excitation | $e + \text{He}_m^* \rightarrow e + \text{He}$ | | $1.099 \times 10^{-17} T_e^{0.31}$ | -19.8 | |
| 11 | e-impact dissociation | $e + \text{He}_2^* \rightarrow e + 2\text{He}$ | | $1.2 \times 10^{-18} T_e^{0.71} \exp\left(\frac{-3.945 \times 10^4}{T_e}\right)$ | -17.9 | |
| 12 | Ion-e recombination | $\text{He}^+ + 2e \rightarrow e + \text{He}_m^*$ | | $5.38 \times 10^{-13} T_e^{-0.5}$ | -4.78 | |
| 13 | Ion-e dissociative recombination | $\text{He}_2^+ + 2e \rightarrow \text{He}_m^* + \text{He} + e$ | | | 0 | |
| 14 | Ion-e dissociative recombination | $\text{He}_2^+ + e + \text{He} \rightarrow \text{He}_m^* + 2\text{He}$ | | | 0 | |
| 15 | Ion-e recombination | $\text{He}_2^+ + 2e \rightarrow \text{He}_2^* + e$ | | | 0 | |
| 16 | Ion-e recombination | $\text{He}_2^+ + e + \text{He} \rightarrow \text{He}_2^* + \text{He}$ | | | 0 | |
| 17 | Hornbeck-Molnar associative ionization | $\text{He}_{\text{ex}}^{**} + \text{He} \rightarrow \text{He}_2^+ + e$ | | 1.5×10^{-17} | 0 (n>3) | |
| 18 | Metastable-metastable associative ionization | $\text{He}_m^* + \text{He}_m^* \rightarrow \text{He}_2^+ + e$ | | 2.03×10^{-15} | -18.2 | |
| 19 | Metastable-metastable ionization | $\text{He}_m^* + \text{He}_m^* \rightarrow \text{He}^+ + \text{He} + e$ | | 8.7×10^{-16} | 2.7×10^{-16} | -15.8 |
| 20 | Ion conversion | $\text{He}^+ + 2\text{He} \rightarrow \text{He}_2^+ + \text{He}$ | | 6.5×10^{-44} | 1.0×10^{-45} | 0 |
| 21 | Metastable-induced association | $\text{He}_m^* + 2\text{He} \rightarrow \text{He}_2^+ + \text{He}$ | | 1.9×10^{-46} | 1.3×10^{-45} | 0 |
| 22 | Metastable-induced dissociative ionization | $\text{He}_m^* + \text{He}_2^* \rightarrow \text{He}^+ + 2\text{He} + e$ | | 5×10^{-16} | | -13.5 |
| 23 | Metastable-induced ionization | $\text{He}_m^* + \text{He}_2^* \rightarrow \text{He}_2^+ + \text{He} + e$ | | 2×10^{-15} | | -15.9 |
| 24 | Dimer-induced dissociative ionization | $\text{He}_2^* + \text{He}_2^* \rightarrow \text{He}^+ + 3\text{He} + e$ | | 3×10^{-16} | | -11.3 |
| 25 | Dimer-induced ionization | $\text{He}_2^* + \text{He}_2^* \rightarrow \text{He}_2^+ + 2\text{He} + e$ | | 1.2×10^{-15} | | -13.7 |
| 26 | He-atom induced Dissociation | $\text{He}_2^* + \text{He} \rightarrow 3\text{He}$ | | 4.9×10^{-22} | | 0 |

3.1.3 Temporal Variation of Spatial-average Plasma Properties

Figure 6 shows a series of temporal variation of several important discharge

properties in a cycle using the complex chemistry, which include: a) the applied voltage, discharge current, dielectric voltage, gap voltage, and accumulated charge densities on both powered and grounded dielectrics, b) the spatial-average concentrations of charged particles and electron temperature, and c) the spatial-average concentrations of excited, metastable non-charged heavy particles. We have divided the first half cycle (rising voltage period) into several distinct modes of discharge, which include long Townsend like discharge (region A), dark current like discharge (region B), primary short Townsend like discharge (region C), and secondary short Townsend like discharge (region D), for the convenience of discussion as described next. In the following, typical detailed distribution of the discharge properties in each region will be presented next to elucidate the underlying physics.

3.1.3.1 Region A - Long Townsend like region

In this region A, the gap voltage decreases with time because of the memory effect as mentioned earlier (shielded by increasing negative and positive accumulated charges at powered and grounded dielectrics, respectively), although the applied voltage increases with time, as shown in Figure 4a. The magnitude of maximum current density is ~ 2.4 mA/cm², which is a typical characteristics of Townsend like discharge and the temporal width is ~ 15 μ s in region A. It is termed as “long” because it lasts for 15 μ s for a cycle period of 50 μ s. At this instant, the electrons and ions are attracted to the anode and cathode, respectively, and the average electron temperature is as high as 7 eV (Figure 4b). In general, the electron density is far less than the molecular helium ion density across the

gap, except in the small region near the anode, which is a typical characteristic of a Townsend like discharge. Correct prediction of the discharge current using the complex plasma chemistry in region A is attributed to the inclusion of channels like Hornbeck-Molnar associative ionization (No. 17 in Table 1), metastable-metastable associative ionization (No. 18 in Table 1) and several dimmer and metastable related ionization channels (No. 21, 23 and 25 in Table 1), which can generate abundant molecular helium ions for producing enough discharge current as compared to the simple plasma chemistry. Thus, the use of complex plasma chemistry by including more heavy particle related channels in the fluid modeling as mentioned in the above can faithfully reproduce the experimental discharge current in the region A.

3.1.3.2 Dark current like discharge

In region B, the gap voltage decreases with decreasing applied voltage and the current density becomes very small (maximal value $\ll 1\text{mA/cm}^2$), which is much smaller than the current in the previous long Townsend-like discharge (Figure 4a). In addition, the magnitude of accumulated charges on both dielectrics begins to decrease gradually, which leads to a slightly decreased dielectric voltage (Figure 4a). This region lasts for only $\sim 3.5\ \mu\text{s}$. Nevertheless, the abundant electrons generated by those previously mentioned ionization channels (in region A) can still be kept inside the gap because of this very small electric field and form the quasi-neutral plasma bulk. After this instant, the electric field begins to increase with increasingly negative gap voltage (Figure 4a), which leads to the increase of electron temperature as can be seen from Figure 4b. By summing up the above

observations, we can conclude that it is a “dark current” like, instead of a glow like, discharge in region B because of the very small discharge current, the very small amount of short-lived excited helium and the very low electron temperature, although abundant charged species with quasi-neutrality plasma bulk still exist in the gap.

3.1.3.3 Primary short Townsend like discharge

In region C, the gap voltage increases rapidly initially from -250 volts up to ~750 volts and remains at this voltage for a period of ~2 μs because the shielding from increasing accumulated charges on dielectric surfaces balances with the increasing applied voltage (Figure 4a). The magnitude of the maximal discharge current is about ~8 mA/cm² and the electron density is much less than the ion density (especially the molecular ion); while the electron temperature is relatively high (~7 eV on the average) (Figure 4b). This is termed as “primary short” because of the period of the discharge is shorter (3-4 μs) and the discharge current is much larger. This short and large discharge current is mainly caused by the very large rate of increase of the applied voltage (pulse; from ~1,500 to ~3,000 volts in less than 1 μs), which in turn causes the gap voltage to increase in a similar fashion. This rapid increase of the voltage attracts a large amount of electrons and molecular ions to move very fast towards the anode and cathode, respectively (Figure 4a). This in turn quickly shields the applied voltage and then after this short current peak the gap voltage keeps at approximately constant value because the shielding caused by the charge accumulation on both dielectrics cancels out the increase of applied voltage.

3.1.3.4 Secondary short Townsend like discharge

In region D, a secondary short Townsend like discharge ($\sim 1-2 \mu\text{s}$) is induced as the applied voltage rapidly decrease from ~ 3500 down to ~ 2400 volts within $1 \mu\text{s}$ (the gap voltage reverses from 500 volts to -500 volts). Corresponding maximal current density is $\sim 5 \text{ mA/cm}^2$. Because of the polarity change of the gap voltage the electrons and ions rapidly accumulate on the grounded (anode) and powered (cathode) dielectric surface respectively, which reduces the magnitude of surface charges on both dielectric surfaces simultaneously, as shown in Figure 4a. This in turn reduces the dielectric voltage. In other words, this short secondary Townsend like discharge is formed due to the rapid gap voltage reversing.

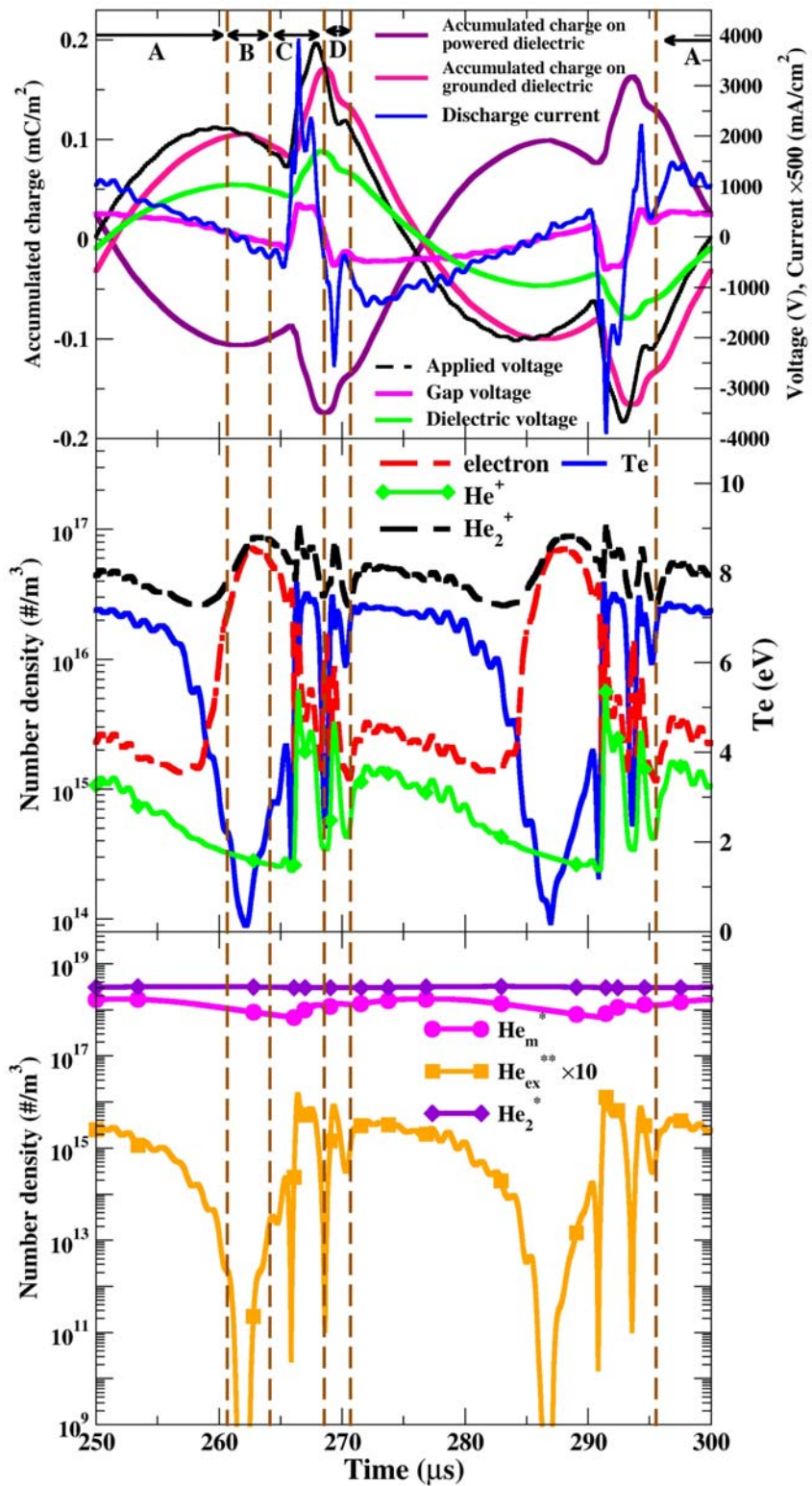


Figure 6. Temporal variation of spatial-averaged plasma properties for the atmospheric pressure helium DBD driven by a distorted-sinusoidal power source (20 kHz).

3.2. Atmospheric Pressure One-Dimension Nitrogen DBD

Parallel-plate nitrogen dielectric barrier discharge (DBD) driven by a realistic distorted-sinusoidal voltage power source (60 kHz) is simulated using a fully-implicit 1D self-consistent fluid modeling code. The results are also compared with the experiments wherever possible. Effects of the gap distance and the dielectric material are considered in the simulations. The N₂ plasma chemistry employed in the present study includes 9 species (electron, N₂, N₂⁺, N₄⁺, $N_2(X^1\Sigma_g^+, \nu = 1-8)$, $N_2(A^3\Sigma_u^+)$, $N_2(B^3\Pi_g)$, $N_2(C^3\Pi_u)$, $N_2(a^1\Sigma_u^-)$) and 31 reactions. This set of nitrogen plasma chemistry includes direct ionization (1), excitation into excited, metastable and vibration states (5), de-excitation (6), recombination (3), associative ionization (3), light emission from excited, metastable states (4) and excitation into vibration states (10).

3.2.1 Discharge structure

Figure 7 shows that comparison of simulated and measured discharged currents of nitrogen DBD driven by a quasi-pulsed power in 6800 V, 0.5 mm gap distance, 60 kHz along with the experimental photo images (0.2 s exposure time) of discharge on the right. It is seen in the figure that the simulations are in good quantitative agreement with the experimental data for all phase of discharge. At atmospheric pressure nitrogen, the associative ionization from metastable nitrogen $N_2(A^3\Sigma_u^+)$ and $N_2(C^3\Pi_u)$ can create the electrons and N₄⁺ to sustain the plasma, therefore the current peak much wide compare to helium narrow peak

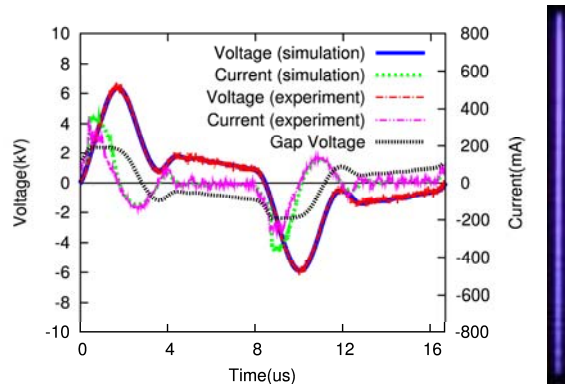


Figure 7. Comparison of simulated and measured discharged currents in 6800 V, 0.5 mm gap distance, 60 kHz along with photo images of discharge at the right.

In Figure 8, the spatial distributions are given at the maximum point of the discharge current. Ion conduction current is higher than that of electron, which is characteristic of Townsend discharge. The total current is the same value between dielectric changes with the time only.

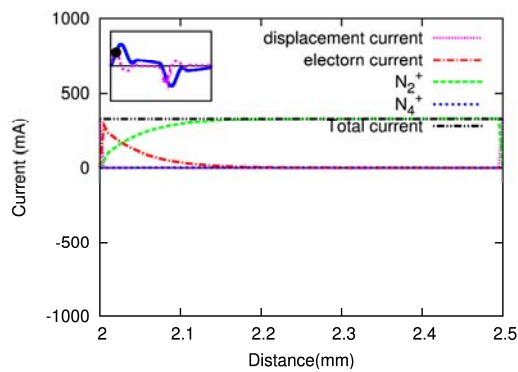


Figure 8. Parts of total discharge current at the maximum discharge current.

The spatial distributions over the discharge gap of the reduced electric field, charges particles density and electric temperature are shown in Figure 9 and 10. In Figure 9, the electron density grows exponentially from cathode to anode and its value is lower than the

ion density. Therefore, there is no quasineutral region. This is the typical feature of the Townsend discharge.

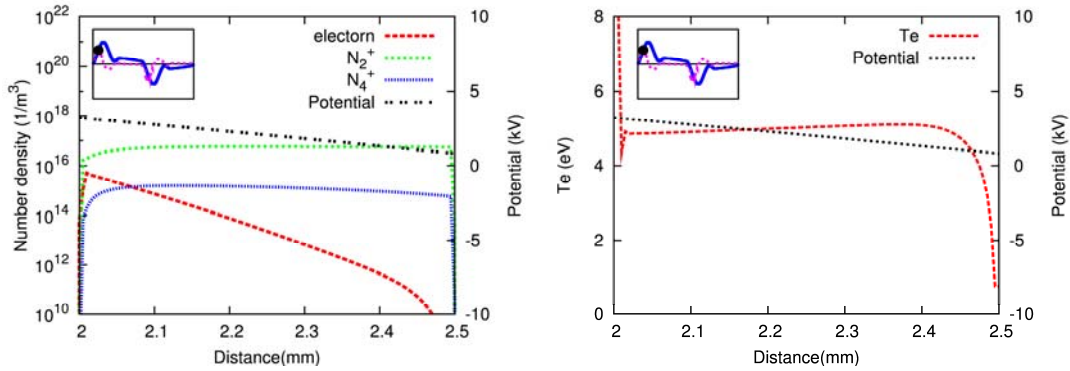


Figure 9. Spatial distributions of electric field, charged particles and electron temperature at the maximum discharge current.

In Figure 10, N_2^+ is found to be most abundant during the breakdown process (same period of those current peaks in Figure 1), while N_4^+ is found to be dominant after the breakdown caused by the associative ionization of excited/metastable nitrogen species.

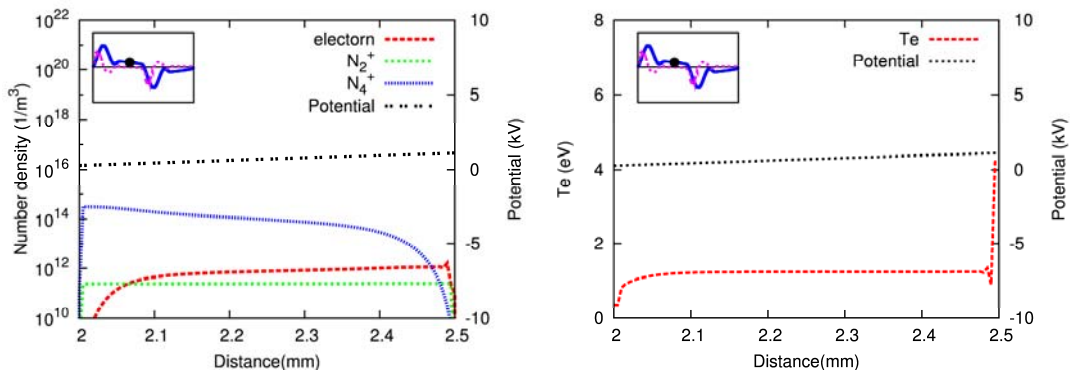


Figure 8. Spatial distributions of electric field, charged particles and electron temperature after the breakdown.

3.2.2 Influence of gap distance

Figure 11 shows that comparison of simulated discharged currents of nitrogen DBD driven by a quasi-pulsed power (60 kHz) for different gap distances (0.5, 0.7, 1.0, 1.2 and 1.4 mm) along with the experimental photo images (from left to right) of discharge on the right.

For the cases of smaller gap (0.5, and 0.7 mm), the simulations demonstrate they are typically homogeneous Townsend-like discharges with much fewer electrons than ions (not shown here). For the case of larger gap ($d=1.0$ and 1.2 mm), the simulation shows it is a glow-like discharge with very high current density during the breakdown phase. This is attributed to the fact that the discharge has transitioned from Townsend-like to filamentary-like (microdischarge). However, this is obviously against the measurements in larger gap non-uniform case as shown in the photo images in Figure 11. This shows that one has to be very cautious about the use of one-dimensional fluid modeling for simulating the non-uniform parallel-plate nitrogen DBD.

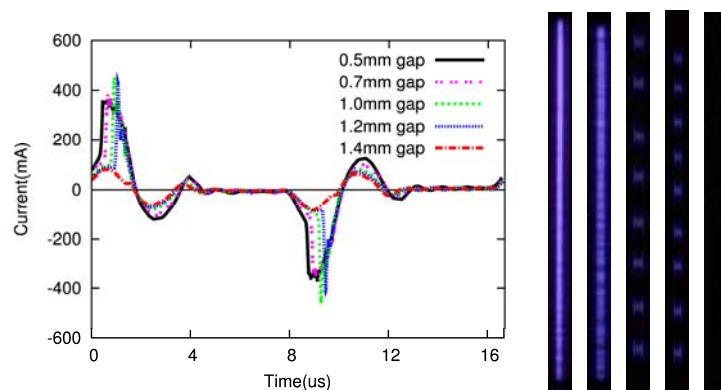


Figure 11. Comparison of different gap distance discharged currents along with photo images of discharge at the right.

3.2.3 Influence of dielectric material

The DBD is generated in the space between two electrodes, each of which is covered with an insulating. The insulating dielectric barrier prevented real currents flowing from the discharge volume to the electrodes and power supply. The calculations are made for two different dielectric materials ceramic ($\epsilon = 12.63$) and quartz ($\epsilon = 4.76$) in 2.0 mm thickness. The gap distance between dielectric is 0.5 mm, and the applied amplitude is 8600 V which can reach the quartz DBD breakdown voltage in 60 kHz frequency. It is seen in figure 10 that the magnitude of the barrier permittivity changes the behavior of the discharge. First, the dielectric accumulated the charge particle and grown with the applied voltage. The maximum accumulated charge is proportional to the permittivity constant of dielectric. When the applied voltage changed the phase from positive to negative voltage, the accumulated particles moved to another side of dielectric immediately. At the same time, those particles marked a great ionization and reached plasma breakdown. Therefore, the larger dielectric constant has more electron seed to ionize and sustain the plasma. The total current also increases with dielectric constant.

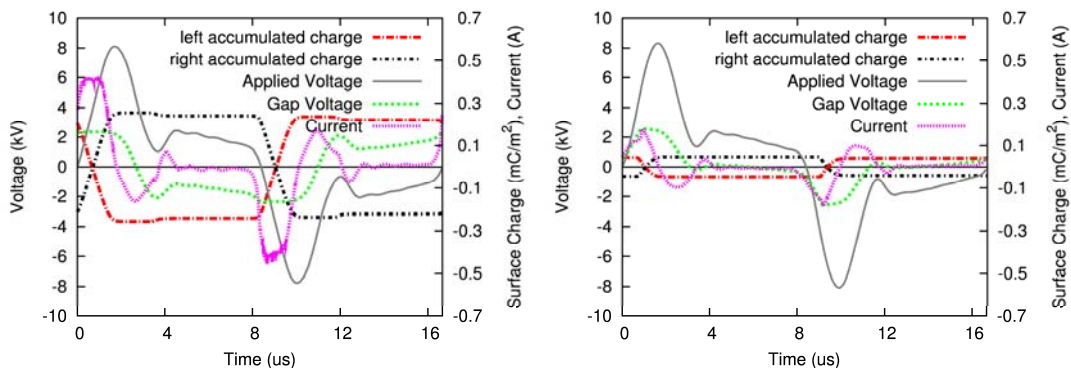


Figure 10. Calculated current, gap voltage, accumulated and applied voltage waveform in

different dielectric material (left) ceramic (right) quartz.

3.3. Atmospheric Pressure Two-Dimension He and Nitrogen DBD

The results shown in the following are adapted from the simulation of a helium gas flowing through two parallel electrode with gap distance of 1 mm and length of 50 mm (Fig. 2), in which the discharge is maintained by a RF power source ($f=13.56$ MHz) with amplitude of 200 Volt. Fig.3 shows the steady-state distribution of flow properties (pressure, density, mass fraction of He and N₂, mean speed, and streamline).

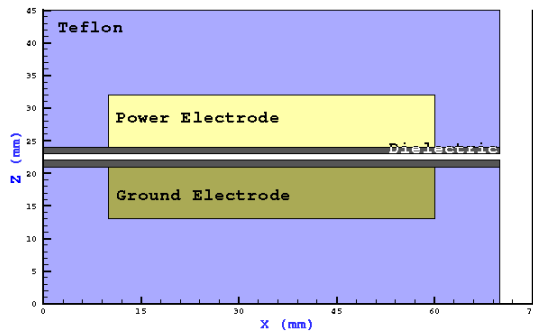
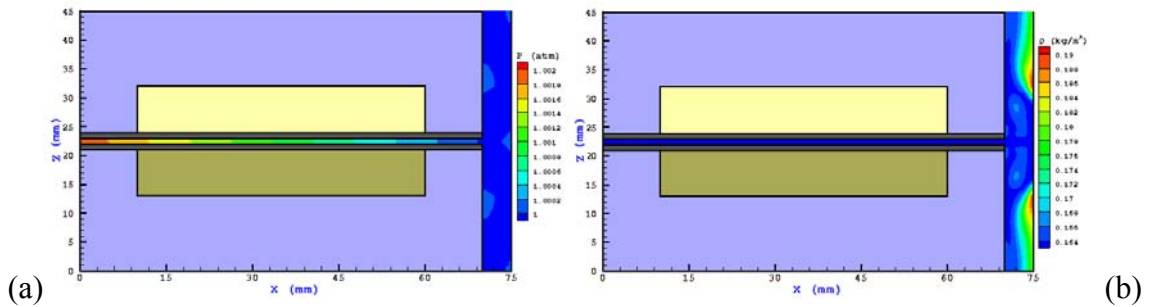


Figure 12. Sketch of Dielectric Barrier Discharge



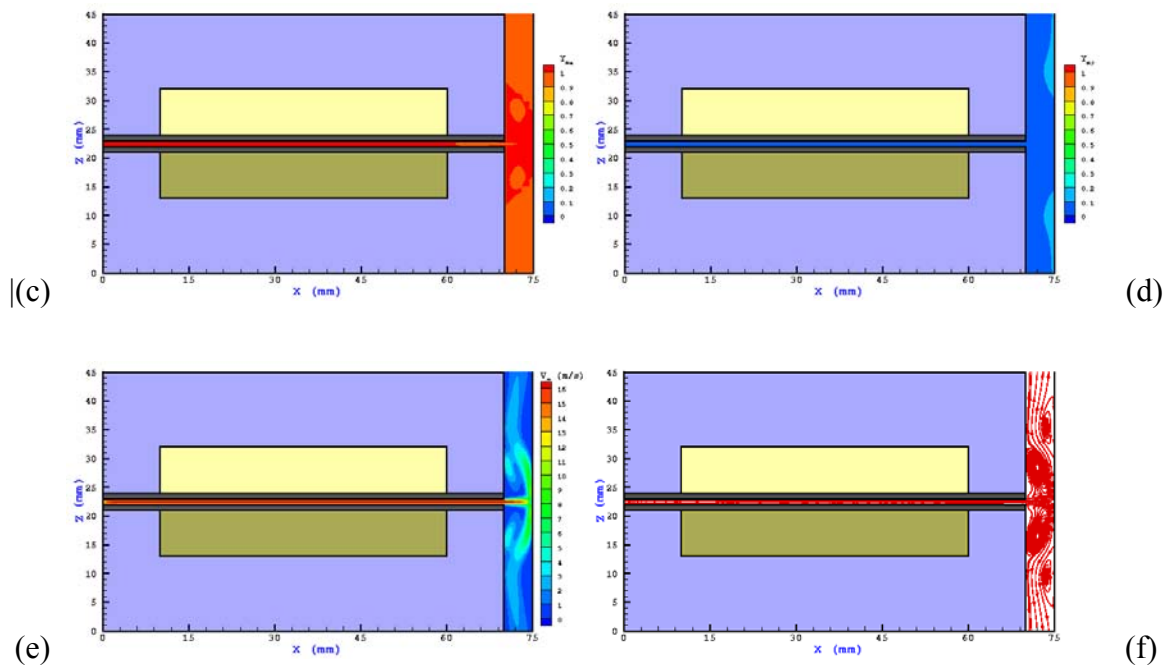


Figure 13. Distribution of (a) pressure, (b) density, (c) mass fraction of He, (d) mass fraction of N₂, (e) mean speed, and (f) streamline.

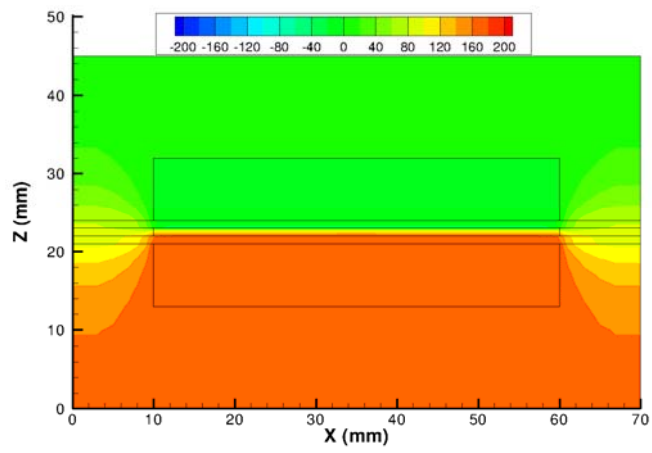
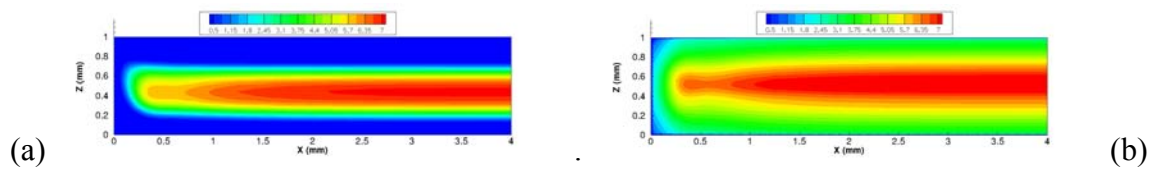


Figure 14. Snapshot of potential distribution at $\Theta=45^\circ$



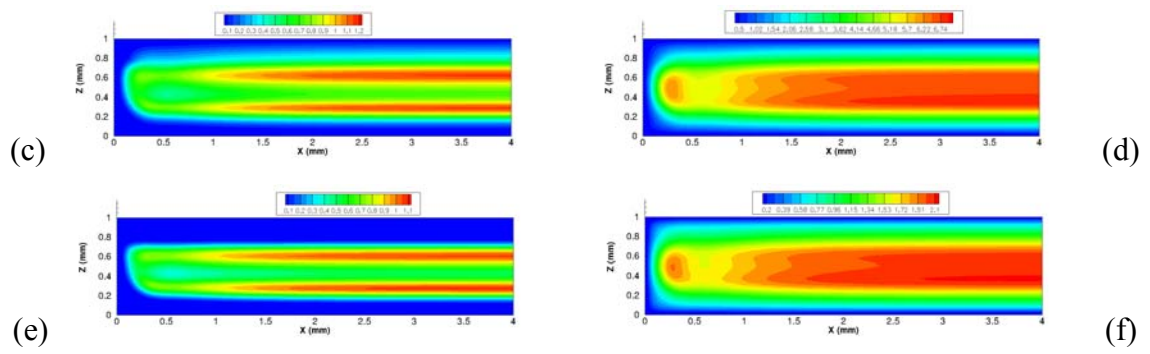


Figure 15. Cycle averaged density distribution along x from 0 to 4 mm: (a) electron (b) He²⁺ (c) He⁺ (d) He meta state (e) He excited state (2) He₂ excited spate.

4. Conclusion Remarks

In the present study, two sets of prototype of fluid modeling and neutral flow solvers were developed using either finite difference method or advanced finite volume method. Results show that these two codes are able to simulate realistic APPJ problems for different and also validated by experiments with different feeding gas and applied power source. The coupling of fluid modeling and Navier-Stokes solver are in progress.

5. References

1. Holyoak, G. R., Wang, S. Q., Liu, Y. H. and Bunch, T. D., 1996, "Toxic Effects of Ethylene Oxide Residues on Bovine Embryos in Vitro," *Toxicol.*, Vol. 108, Issue 1-2, pp. 33-38.
2. Lucas, A. D., Merritt, K., Hitchins, V. M., Woods, T. O., NcMamee, S. G., Lyle, D. B. and Brown, S. A., 2003, "Residual Ethylene Oxide in Medical Devices and Devices Material," *J. Biomed. Mater. Res. Part B: Appl. Biomater.*, Vol. 66B, Issue 2, pp. 548-552.
3. Moisan, M., Barbeau, J., Moreau, S., Pelletier, J., Tabrizian, M. and Yahia, L. H., 2001, *Int. J. Pharmac.*, Vol. 226, Issue 1-2, pp. 1-21.
4. Deng, X. T., Shi, J. J. and Kong, M. G., 2006, "Physical Mechanisms of Inactivation of *Bacillus subtilis* Spores Using Cold Atmospheric Plasmas," *IEEE Trans. Plasma Sci.*, Vol. 34, Issue 4, pp. 1310-1316
5. Lee, K., Paek, K. H., Ju, W. T. and Lee, Y., 2006, "Sterilization of Bacteria, Yeast, and Bacterial Endospores by Atmospheric-Pressure Cold Plasma Using Helium and Oxygen," *J. Microbiol.*, Vol. 44, Issue 3, pp. 269-275.
6. Lerouge, S., Wertheimer, M. R., Marchand, R., Tabrizian, M. and Yahia, L., 2000, "Effect of Gas Composition on Spore Mortality and Etching During Low-Pressure Plasma Sterilization," *J. Biomed. Mater. Res.*, Vol. 51, Issue 1, pp. 128-135.
7. Sharma, A., Pruden, A., Stan, O. and Collins, G. J., 2006, "Bacterial Inactivation Using an RF-Powered Atmospheric Pressure Plasma," *IEEE Trans. Plasma Sci.*, Vol. 34, Issue 4, pp. 1290-1296.
8. Sun, Y. Z., Qiu, Y. C., Nie, A. L. and Wang, X. D., 2007, "Experimental Research on Inactivation of Bacteria by Using Dielectric Barrier Discharge," *IEEE Trans. Plasma Sci.*, Vol. 35, Issue 5, pp. 1496-1500
9. Hippler, R., Kersten, H., Schmidt, M. and Schoenbach, K. H., 2008, Low temperature plasmas: fundamentals, 2nd ed., *Wiley*, New York, pp. 821-835
10. Laroussi, M., Richardson, J. P. and Dobbs, F. C., 2002, "Effects of Nonequilibrium Atmospheric Pressure Plasmas on the Heterotrophic Pathways of Bacteria and on Their Cell Morphology," *Appl. Phys. Lett.*, Vol. 81, Issue 4, pp. 772-774

11. Nilsson, H., and Davidson, L., "CALC-PVM: A Parallel SIMPLEC Multiblock Solver for Turbulent Flow in Complex Domain", Int. rep. 98/12, Dep. of Thermo and Fluid Dynamics, Chalmers University of Technology, Goteborg.
12. Shterev, K.S., Stefanov, S.K., "Pressure based finite volume method for calculation of compressible viscous gas flows", J. Comp. Phys. n.229, pp 461-480, 2010.
13. Karki, K.C. and Patankar, S.V., "Pressure Based Calculation Procedure for Viscous Flows at all Speeds in Arbitrary Configurations," AIAA J., Vol. 27, pp. 1167-1174, 1989.
14. Shang, H.M., Chen, Y.S., Liaw, P., Shih, M.S. and Wang, T.S., "Numerical Modeling of Spray Combustion with an Unstructured Grid Method", AIAA Paper 95-2781, 1995.
15. BOLSIG <http://www.siglo-kinema.com/bolsig.htm>
16. Yuan X and Raja L L 2003 *IEEE T. Plasma Sci.* **31** 495
17. Ellis H W, Pai R Y, McDaniel E W, Mason E A and Viehland L A 1976 *Atomic Data Nucl. Data Tables* **17** 177-10
18. Hung C T, Hu M H, Wu J S and Hwang F N 2007 *Comput. Phys. Commun.* **177** 138-39
19. Balay S, Buschelman K, Gropp W D, Kaushik D, Knepley M G, McInnes L C, Smith B F and Zhang H 2009 <http://www.mcs.anl.gov/petsc>

6.Related Publications

1. C.-T. Hung, Y.-M. Chiu, F.-N. Hwang, **J.-S. Wu***, “Development of a Parallel Implicit Solver of Fluid Modeling Equations for Gas Discharges,” *Computer Physics Communications*, Vol. 182, pp. 161-163, January 2011.
2. Y.-M. Chiu, C.-T. Hung, F.-N. Hwang, M.-H. Chiang, **J.-S. Wu***, S.-H. Chen, “Effect of Plasma Chemistry on the Simulation of Helium Atmospheric-Pressure Plasmas,” *Computer Physics Communications*, Vol. 182, pp. 167-169, January 2011.
3. K.-W. Cheng, C.-T. Hung, M.-H. Chiang, F.-N. Hwang, **J.-S. Wu***, “One-dimensional Simulation of Nitrogen Dielectric Barrier Discharge Driven by a Quasi-Pulsed Power Source and Its Comparison with Experiments,” *Computer Physics Communications*, Vol. 182, pp. 164-166, January 2011.
4. M.R. Smith, K.-M. Lin, C.-T. Hung, Y.-S. Chen and **J.-S. Wu***, “Development of an Improved Spatial Reconstruction Technique for the HLL Method and Its Applications,” *Journal of Computational Physics*, Vol. 230, January, pp. 477–493, 2011.
5. C.-T. Hung, Y.-M. Chiu, F.-N. Hwang, M.-H. Chiang, **J.-S. Wu*** and Y.-C. Wang, “Investigation of Helium Dielectric Barrier Discharge Driven by a Realistic Distorted-Sinusoidal Voltage Power Source,” *Plasma Chemistry and Plasma Processing* (**accepted**, October 15, 2010).
6. M.-H. Hu, **J.-S. Wu*** and Y.-S. Chen, ”Development of a Parallelized 2D/2D-Axisymmetric Navier-Stokes Equation Solver for All-Speed Gas Flows,” *Computers & Fluids* (special issue for ParCFD 2010, **submitted** on September 24, 2010).